Chemical Engineering Journal 457 (2023) 141289

Contents lists available at ScienceDirect

Chemical Engineering Journal

journal homepage: www.elsevier.com/locate/cej

Inkjet-printed MoS_2-based 3D-structured electrocatalysts on Cu films for ultra-efficient hydrogen evolution reaction

Pei-Zhen Li [a,1], Na Chen [a,1], Ammar Al-Hamry [b], Evgeniya Sheremet [c], Ran Lu [a], Yi Yang [a], Olfa Kanoun [b], Reinhard R. Baumann [d], Raul D. Rodriguez [c,*], Jin-Ju Chen [a,*]

[a] School of Materials and Energy, University of Electronic Science and Technology of China, Chengdu 610054, P. R. China
[b] Professorship of Measurement and Sensor Technology, Chemnitz University of Technology, Chemnitz 09126, Germany
[c] Tomsk Polytechnic University, 30 Lenin Ave, Tomsk 634050, Russia
[d] Digital Printing and Imaging Technology, Chemnitz University of Technology, Chemnitz 09126, Germany

ARTICLE INFO

Keywords:
Inkjet printing
Transition metal dichalcogenides (TMDs)
MoS_2
Hydrogen evolution reaction (HER)
3D architecture

ABSTRACT

2D transition metal dichalcogenides (TMDs) are emerging as promising alternative electrocatalysts for hydrogen evolution reaction (HER). However, key challenges are the limited density of available activity sites and poor electron accessibility. Herein, Cu film supported MoS_2-based electrocatalyst with partial 1T phase and 3D architecture is constructed by inkjet printing. We aim to investigate if this configuration could provide largely exposed edge sites and enhance electron transfer for ultra-efficient hydrogen production. Towards this end, an ink containing few-layer MoS_2 nanosheets and reduced graphene oxide (RGO) is firstly prepared by liquid-phase exfoliation, in which semiconducting 2H-MoS_2 is partially transformed to metallic 1 T-MoS_2. We demonstrate that 1) nanosized few-layer MoS_2 spatially patterned by inkjet-printing provides sufficient active site exposure, 2) the 1T-MoS_2 and RGO conductive network reduce the charge-transfer impedance, and 3) the Cu support enhances the catalyst-electrode charge injection. Our all-in-one structure exhibits outstanding HER activities with low overpotential (51 mV at 10 mA cm^{-2} and 126 mV at 100 mA cm^{-2}) and very low Tafel slope (32 mV dec^{-1}). Also, the as-engineered electrode demonstrates ultrahigh cathodic current density. This work provides a facile, inexpensive, and scalable way for designing and fabricating TMDs-based electrocatalysts with excellent HER activity.

1. Introduction

The increasing demand for energy in our society stimulated intensive research on developing sustainable and renewable energy sources to lessen our dependence on fossil fuels.[1–3] Hydrogen is one of the most promising energy carriers in future technologies. However, hydrogen generation presents some challenges of its own. Water splitting in the form of electricity by hydrogen evolution reactions (HER) has been proposed as a practical way for hydrogen fuel production.[4–6] In HER, electrocatalysts are widely used to maximize the efficiency of the electrochemical reactions by lowering their overpotentials and accelerating the reaction rates. Although noble metals, such as platinum, exhibit high electro-activity towards HER,[7] the high cost and scarcity of noble metals are severe barriers to their large-scale and sustainable application. Therefore, developing low-cost and earth-abundant catalysts with performance comparable to that of Pt-group metals is one of the most sought goals in catalysis.

2D layered transition metal dichalcogenides (TMDs) with the general formula MX_2 (M is a transition metal, and X is typically S or Se) were demonstrated as appealing electrocatalysts for HER.[8–13] Theoretical and experimental results showed that the unsaturated X-edges on the edge planes of the semiconducting 2H phase of TMDs were electrocatalytically active for HER, and a strong correlation between the catalytic activity and the number of edges was verified. [14–19] This selective high-activity of edges has rapidly triggered the development of nanostructured TMDs with a high concentration of edge sites. [20] Among these efforts, the most substantial progress is happening for molybdenum disulfide (MoS_2) nanostructures,[21] including nanoparticles,[22] nanosheets,[23,24] nanoflowers,[25,26] and quantum dots,[27] all showing enhanced electrochemical HER activity. In

* Corresponding authors.
E-mail addresses: raul@tpu.ru (R.D. Rodriguez), jinjuchen@uestc.edu.cn (J.-J. Chen).
[1] These authors contributed equally to this work.

https://doi.org/10.1016/j.cej.2023.141289
Received 3 October 2022; Received in revised form 22 December 2022; Accepted 2 January 2023
Available online 3 January 2023

addition to tailoring MoS_2 with nanometer size, designing MoS_2 systems with engineered microstructure has also been explored to expose more edge sites like in mesoporous MoS_2 with a double-gyroid morphology, [28] synthesizing MoS_2-based 3D hierarchical structures by space-confined method,[29] and constructing nanostructured MoS_2 on a 3D-structured substrate.[30] Nevertheless, the HER catalytic activity of those MoS_2-based systems remains much inferior to that of Pt.

Besides the number of exposed active sites, electron accessibility is another critical factor contributing to the electrocatalytic activity of MoS_2.[31,32] 2H-MoS_2 possesses poor intrinsic conductivity due to its semiconducting character. Therefore, the hopping transfer of electrons in the vertical direction of 2H-MoS_2 layers reduces HER kinetics significantly.[33,34] In this context, the fabrication of ultrathin MoS_2 nanosheets is a feasible solution for low HER kinetics.[35,36] Also, MoS_2 combined with carbon-based conductive materials (such as reduced graphene oxide (RGO)[37,38] and graphite felt[39]) was shown to help overcome this electrical conductivity limitation. Besides the significant role of edges, a strong correlation between the electronic structure of MoS_2 and its HER catalytic activity has been demonstrated.[40] It was found that the metallic 1T-MoS_2 phase exhibits a much higher HER activity than the semiconducting 2H-MoS_2.[41,42] Although these efforts have effectively enhanced the HER activity of MoS_2, the complex processes involved make them challenging to implement at a large scale.

In the electrocatalytic process, the electrode/current collector is responsible for charge carrier injection to the catalyst materials while also acting as mechanical support. Given its charge carrier injection function, the contact resistance between the current collector and catalyst is crucial to HER performance. In practice, a catalytic electrode for HER usually requires an additional polymer binder to immobilize catalysts on the current collector. These binders often have the negative effect of introducing an extra resistance between catalysts and the current collector, which degrades the overall catalytic performance. A theoretical investigation suggested that the support interaction can be used to tune the HER catalytic activity of MoS_2 by changing the coupling between the substrate and the catalyst.[43] Experimental results demonstrated that the enhanced electronic coupling could facilitate charge injection from the underlying electrode to the active sites, improving the intrinsic catalytic performance of 2H-MoS_2 comparable to 1T-MoS_2.[44] Hence, binder-free electrodes with catalysts assembled onto a conductive substrate are now receiving a considerable amount of attention, with Au,[22] Ni,[45] carbon cloth,[46,47] or graphite paper [48] as the current collector. It is well known that the contact between the metal electrode and MoS_2 naturally forms a Schottky barrier. The Schottky barrier height (SBH) is a critical factor in determining the contact resistance in the metal-MoS_2 system, which significantly affects electron mobility. According to the Schottky-Mott model, the SBH could be estimated as the difference between the Fermi level of the metal electrode and the conduction band minimum of MoS_2. When SBH decreases to zero or gets further negative, Schottky contact changes into ohmic contact. An ideal electrode material should have a work function as close as possible to or lower than the electron affinity of MoS_2. Cu work function is 4.65 eV,[49] which is slightly lower than the electron affinity (4.80 eV) of multilayer MoS_2.[50] Surprisingly, given this close match, Cu is rarely used as an electrode in combination with MoS_2 for electrochemical hydrogen evolution.

In this work, we address these issues and develop a facile strategy to realize a MoS_2-based electrocatalyst with a large density of exposed edge sites, partial 1T-phase MoS_2, reduced charge-transfer impedance, and enhanced electron injection. Polyvinylpyrrolidone (PVP) and RGO were introduced into MoS_2 dispersion for liquid-phase exfoliation to prepare a MoS_2/PVP/RGO ink. PVP promoted the generation of nanosized few-layer MoS_2 and induced the 2H-to-1T phase transition of MoS_2. 3D MoS_2/PVP/RGO microstructures were constructed on Cu film by inkjet printing. This fabrication method made possible the spatial configuration of catalysts in favor of a high density of exposed edge sites. Simultaneously, we exploited the RGO component to form a conductive network that facilitated the electron transfer between the active edge sites and the Cu support. Meanwhile, the Cu support enhanced the electrode-catalyst charge injection. This integrated structure resulted in a novel architecture with dramatically-improved HER catalytic activity.

2. Experimental section

2.1. Materials

All chemical reagents were of analytical grade purity and used as-purchased. MoS_2, PVP (PVP-K30, Mw≈40,000), absolute ethanol (99.7 wt%), and sulfuric acid (H_2SO_4, 98 %) were purchased from Chengdu Kelong Chemical Co., ltd (Chengdu, China). RGO was purchased from Sichuan Huantan Tech Co., ltd (Chengdu, China). Teslin paper (PPG Industry, USA) with a thickness of 356 μm and an RMS surface roughness of 0.61 μm was used as the substrate (the surface morphology is shown in **Fig. S1**, Supporting Information). Deionized water with an electrical conductivity of less than 0.055 μS cm^{-1} was used in the experiments.

2.2. Preparation of Inks

Taking the MoS_2/PVP/RGO ink as an example, the preparation process is described as step 1 in Fig. 1. A mixed solution of 50 vol% ethanol and 50 vol% deionized water (named as mixed solvent) was firstly prepared as the solvent for the exfoliation of bulk MoS_2. 10 mg mL^{-1} of bulk MoS_2, 2 mg mL^{-1} of PVP, and 1 mg mL^{-1} of RGO were successively dispersed in the mixed solvent under magnetic stirring to form a homogeneous mixture. Then the MoS_2 nanostructures were obtained after ultrasonic exfoliation for 48 h at room temperature, in which RGO nanostructures were also fully dispersed in the obtained dispersion. Afterward, the dispersion was centrifuged for 15 min at a speed of 7500 rpm. The resulting supernatant was collected and preserved as the ink for inkjet printing. MoS_2 and MoS_2/PVP inks were also prepared using the same initial concentration of raw materials.

2.3. Preparation of Catalytic Working Electrode

A thin Cu film on Teslin paper with an electrical conductivity of about 4.0×10^7 S m^{-1} was fabricated by a combination of inkjet printing and electroless deposition, as demonstrated in our previous work [51] (step 2 in Fig. 1). The prepared ink was deposited on the Cu support by inkjet printing using a commercially available drop-on-demand Epson L310 desktop printer. The printing was conducted with the "best photo" print quality of 1440 dots per inch (dpi). For example, take the formation of a 3D MoS_2/PVP/RGO architecture obtained by printing a 5×5 mm^2 planar square-shaped graphic with 10 printing passes on the Cu film using the MoS_2/PVP/RGO ink, followed by printing a square-spiral pattern on the previously-printed square using again 10 printing passes (step 3 in Fig. 1, denoted patterned electrode). A homogeneous planar square of 5×5 mm^2 formed using the MoS_2/PVP/RGO ink with 20 printing passes was also prepared for comparison (denoted planar electrode). The printing passes for planar MoS_2 or MoS_2/PVP electrodes were adjusted to ensure that the amount of MoS_2 in the three electrodes was consistent. Patterned MoS_2 or MoS_2/PVP electrode was prepared using a similar method to the patterned MoS_2/PVP/RGO electrode, in which printing passes for the bottom plane and top pattern are both half of the total passes.

2.4. Materials Characterization

Optical microscope images of samples were obtained using an optical microscope (Sunny SZM, China). The morphology of samples was observed by a scanning electron microscope (SEM, JEOL JSM-6490LV, Japan). Energy-dispersive X-ray spectroscopy (EDS, Genesis 2000 XMS, Japan) was used to obtain elemental mapping analysis. Detailed

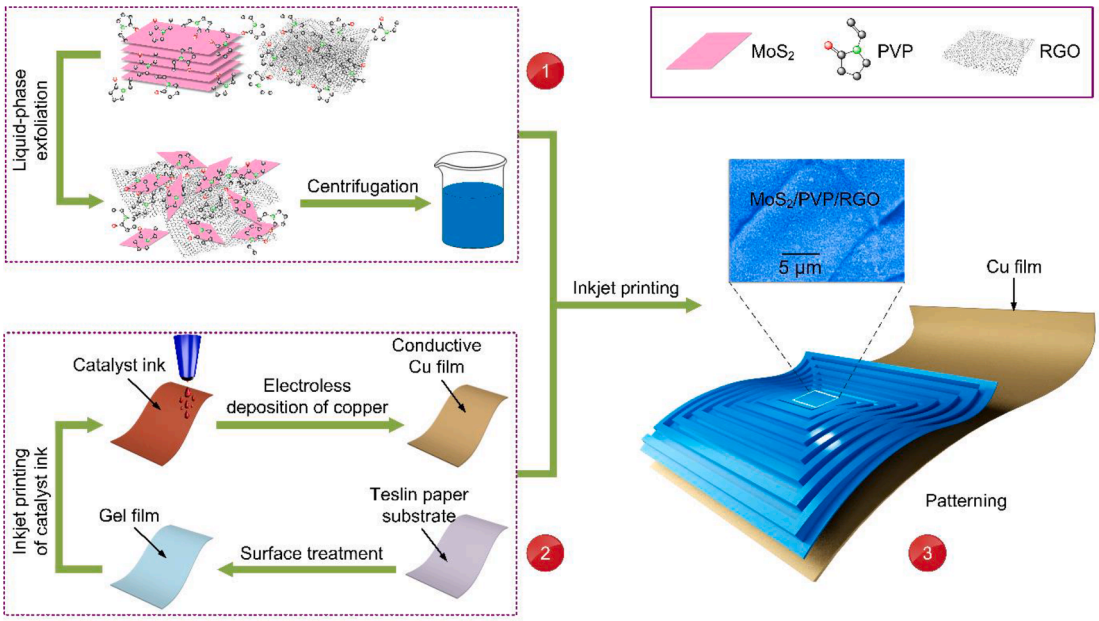

Fig. 1. General scheme for the preparation of catalytic electrodes with spatial patterning *via* inkjet printing. The preparation process of MoS_2/PVP/RGO ink is described in step 1, during which PVP and RGO were introduced into MoS_2 dispersion for a liquid-phase exfoliation of bulk MoS_2, and then the centrifugation was done to obtain MoS_2/PVP/RGO ink. The fabrication of conductive Cu film on Teslin paper (step 2) was described in detail in our previous work. [51] A catalytic electrode was constructed via planar printing followed by graphic printing of the MoS_2/PVP/RGO ink, thus forming a spatial pattern of MoS_2/PVP/RGO (step 3).

microstructure investigation was performed using transmission electron microscopy (TEM, JEOL-2100F, Japan). Ultraviolet–visible (UV–vis) absorption spectra were recorded on a UV-2450 spectrophotometer (Shimadzu, Japan). Raman spectra of samples were acquired on a WITec alpha300 R system (WITec Company, Germany) under 488 nm laser excitation. X-ray photoelectron spectroscopy (XPS) was carried out on a Phi-5000 (Ulvac-Phi, Japan) fitted with an Al Kα radiation source. The crystallinity of materials was characterized using an X-ray diffractometer (Bede-D1, UK) with Cu Kα radiation ($\lambda = 0.15405$ nm).

2.5. Electrochemical Testing

Electrochemical measurements were performed using a CS2350 electrochemical workstation (Wuhan Corrtest, China) in a three-electrode configuration with platinum gauze and Ag|AgCl as the counter electrode and the reference electrode, respectively. 0.5 M H_2SO_4 was used as the electrolyte solution, which was degassed with Ar for 30 min before use. The working electrodes were pre-conditioned for 20 cycles prior to any measurements. The potential difference between the working electrode and the Ag|AgCl reference electrode was converted to the potential versus the reversible hydrogen electrode (RHE) using the equation: $E_{RHE} = E_{Ag|AgCl} + 0.059\ pH + E^0_{Ag|AgCl}$, in which $E^0_{Ag|AgCl}$ is the standard potential of Ag|AgCl at 25 °C (0.1976 V). Linear sweep voltammetry (LSV) was conducted at a scan rate of 5 mV s^{-1} to obtain polarization curves, and polarization curves were iR-corrected. As a reference point, the catalytic performance of 20 % Pt/C electrocatalysts was tested on a glassy carbon electrode under the same conditions. Cyclic voltammetry (CV) experiments were carried out between 0 V and 0.15 V vs RHE. Electrochemical impedance spectroscopy (EIS) was performed with the working electrode biased at −0.20 V over the frequency range 10^5 Hz to 10^{-2} Hz at an AC voltage of 10 mV. The HER stability of the MoS_2/PVP/RGO catalyst was evaluated by a continuous sweep for 5000 cycles between −0.3 V and 0.1 V vs RHE at 5 mV s^{-1}, and a frit was used to separate the MoS_2/PVP/RGO catalyst from the Pt counter-electrode to avoid the influence of Pt dissolution.

2.6. Density functional theory (DFT) calculations

We carried out the DFT calculations to study the electronic properties of samples by using the Vienna ab-initio simulation package (VASP). The interaction of electron and ion was described by the projector augmented wave (PAW) pseudopotentials. The Perdew-Burke-Ernzerhof (PBE) generalized gradient approximation (GGA) was used to represent the electronic exchange and correlation. A 20 Å vacuum layer was introduced to avoid spurious interaction between periodic images. The Brillouin zone was sampled by $4 \times 4 \times 1$ and $3 \times 3 \times 1$ Monkhorst-Pack k-point grids for Cu-MoS_2 contact and Cu-RGO-MoS_2 contact, respectively. A plane wave cutoff of 450 eV was used. Each structure was totally relaxed using a conjugate gradient scheme until the forces and energy converged to 0.03 eV $Å^{-1}$ and 10^{-4} eV, respectively.

3. Results and discussion

3.1. Morphology and Structure

It has been demonstrated that PVP plays the role of surfactant-assisted exfoliation,[52] and RGO can restrain the restacking of MoS_2 in the c-direction.[53] These factors contribute to the ink containing MoS_2 with few-layer and nanosized dimensions. More importantly, the MoS_2/PVP and the MoS_2/PVP/RGO inks are highly stable, without any precipitation during storage for over three months in ambient conditions (**Fig. S2**). This is remarkable stability, especially considering that the MoS_2 ink is stable for no longer than half a month (evidenced by visible sediments and delamination). Undoubtedly, the PVP added to MoS_2/PVP and MoS_2/PVP/RGO inks contributes to long-term storage stability. Such long-term stability is a critical prerequisite for inkjet printing. In addition, the catalyst with PVP has better hydrophilicity than without PVP (**Fig. S3**), which will contribute to the improvement of HER with low mass transfer resistance. After printing with MoS_2/PVP/RGO ink for 20 passes, a planar pattern was formed on the Cu support. The morphology, thickness, and elements distribution of the MoS_2/PVP/RGO layer are shown in **Fig. S4**.

The morphology and structure of the obtained MoS_2, MoS_2/PVP, and MoS_2/PVP/RGO are shown in Fig. 2. It can be noted that the dimension

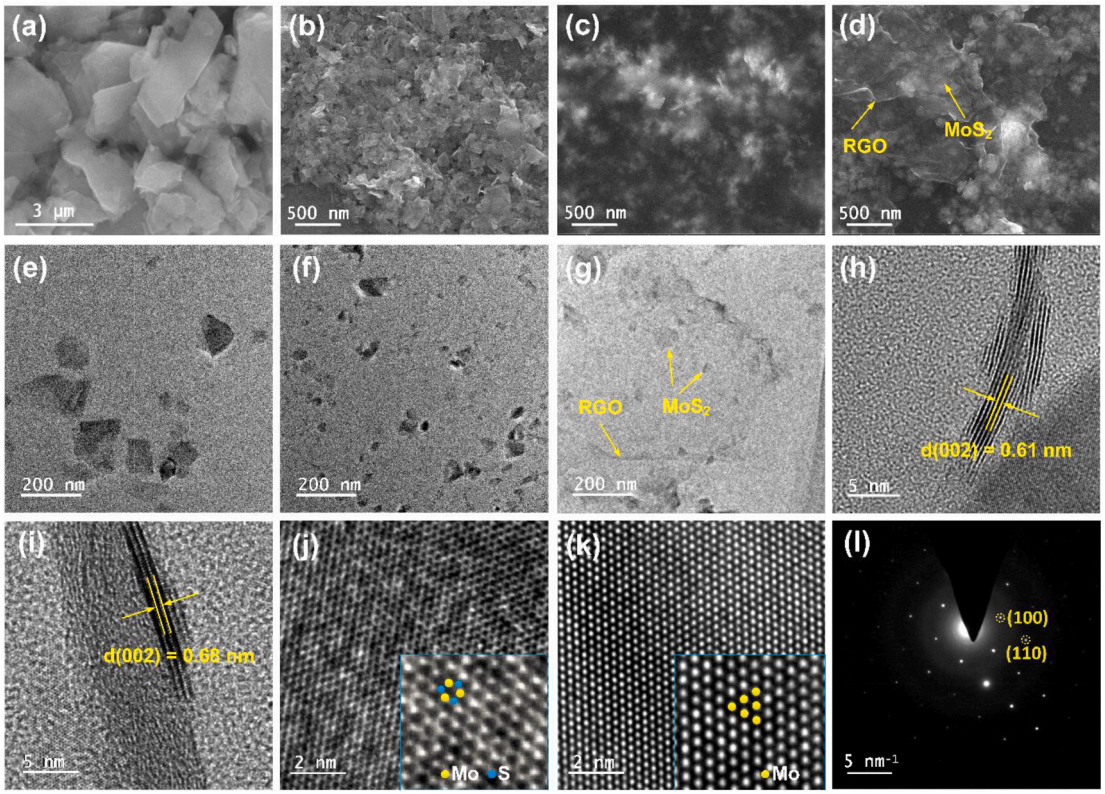

Fig. 2. SEM images of (a) bulk MoS_2, (b) exfoliated MoS_2, (c) MoS_2/PVP, and (d) MoS_2/PVP/RGO. TEM images of (e) pure MoS_2, (f) MoS_2/PVP, and (g) MoS_2/PVP/RGO nanostructures. HRTEM images of (0 0 2) planes for (h) pure MoS_2 and (i) MoS_2/PVP/RGO. HRTEM images of (j) pure MoS_2 and (k) MoS_2/PVP/RGO further show their microstructures. The yellow and blue balls represent Mo and S atoms in the corresponding zoomed-in views, respectively. (l) SAED pattern from MoS_2/PVP/RGO nanosheet showing the hexagonal symmetry of the atomic arrangement.

of exfoliated MoS_2 sheets (Fig. 2b) is much smaller than that of bulk MoS_2 (Fig. 2a), and further dimension reduction (even to the nanoparticle level) can be observed with the addition of PVP (Fig. 2c and 2d). Furthermore, MoS_2 nanostructures are fully surrounded by RGO, as shown in Fig. 2d. TEM images (Fig. 2e-g) show that the lateral size of MoS_2 nanostructures decreases from more than one hundred nanometers for the pure MoS_2 to tens of nanometers for the MoS_2/PVP and the MoS_2/PVP/RGO, indicating the facilitating role of PVP in exfoliating bulk MoS_2 to nanostructures. High-resolution TEM (HRTEM) images in Fig. 2h and 2i show the interplanar crystal spacing of MoS_2. A lattice

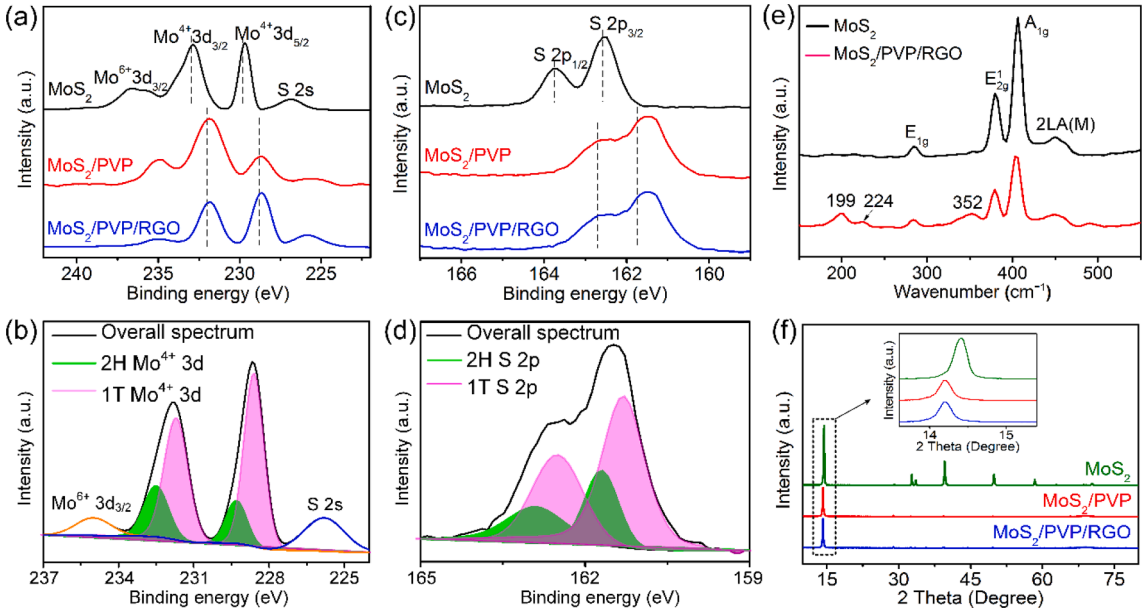

Fig. 3. (a) XPS spectra of Mo 3d for MoS_2, MoS_2/PVP and MoS_2/PVP/RGO. (b) Deconvoluted XPS spectra of Mo 3d for MoS_2/PVP/RGO. (c) XPS spectra of S 2p for MoS_2, MoS_2/PVP and MoS_2/PVP/RGO. (d) Deconvoluted XPS spectra of S 2p for MoS_2/PVP/RGO. (e) Raman spectra of MoS_2 and MoS_2/PVP/RGO. (f) XRD patterns of MoS_2, MoS_2/PVP and MoS_2/PVP/RGO samples.

fringe spacing of 0.61 nm attributed to the (0 0 2) planes and more than eight layers are clearly observed from the pure MoS_2 sample in Fig. 2h, while a lattice fringe spacing of 0.68 nm and as low as four layers for the MoS_2/PVP/RGO sample are shown in Fig. 2i. We attribute the interplanar spacing increase along the c-axis direction to the action of PVP on MoS_2 interlayers. The reduced lateral size results in higher exposure of active sites, and the RGO layers surrounding MoS_2 promote electron transfer, making MoS_2/PVP/RGO a very promising HER catalyst. HRTEM images in Fig. 2j for pure MoS_2 and Fig. 2k for MoS_2/PVP/RGO further display the ordered crystalline arrangement of MoS_2 nanosheets. The honeycomb lattice (trigonal prismatic coordination) and trigonal lattice (octahedral coordination) can be clearly observed from the zoom-in HRTEM images in Fig. 2j and 2k, presenting the 2H and 1T crystal phase[54], respectively. The selected area electron diffraction (SAED) pattern of the MoS_2/PVP/RGO nanosheet in Fig. 2l confirms the hexagonal symmetry of the atomic arrangement.

The phase composition of MoS_2 nanostructures in the ink was characterized by XPS, and the results are shown in Fig. 3. All spectra were calibrated by the C 1s peak located at 284.50 eV.[41] As shown in Fig. 3a, a Mo $3d_{5/2}$ peak at 229.5 eV is observed for the pure MoS_2 sample, revealing the existence of Mo^{4+} species of 2H-MoS_2.[41,54] The binding energy of Mo $3d_{5/2}$ for MoS_2/PVP and MoS_2/PVP/RGO samples shifts to 228.6 eV as a consequence of electronic structure change due to MoS_2 phase transition from 2H to 1T. Mo $3d_{3/2}$ peaks with a + 6 oxidation state are observed in all samples, which is attributed to slight oxidation during sample preparation.[55] For the MoS_2/PVP and the MoS_2/PVP/RGO samples, the broad Mo $3d_{5/2}$ peak can be divided into two independent peaks after deconvolution. Take MoS_2/PVP/RGO as an example, these two peaks are located at 229.5 and 228.6 eV with a binding energy separation around 0.9 eV (Fig. 3b), representing the 2H and the 1T MoS_2 oxidation states, respectively.[37,41] We observe from the peak area that the 1T-MoS_2 phase is dominant. MoS_2 S $2p_{3/2}$ peak at 162.5 eV shifts to 161.5 eV for the MoS_2/PVP and the MoS_2/PVP/RGO samples (Fig. 3c). This change implies the 2H-to-1T transition evidenced after the deconvolution of S $2p_{3/2}$ into two peaks for the MoS_2/PVP/RGO sample (Fig. 3d).[40] The transition to metallic 1T-MoS_2 benefits the catalytic performance due to an enhanced charge transfer kinetics in this electrically conductive MoS_2 phase.

Raman spectroscopy results in Fig. 3e confirm the phase transition of the exfoliated sample. For the pure MoS_2, the Raman spectrum displays characteristic peaks at 285, 378, 405, and 450 cm^{-1} arising from the E_{1g}, E^1_{2g}, and A_{1g} and longitudinal acoustic phonon modes of 2H-MoS_2, respectively [56]. There are three additional peaks at 199, 224, and 352 cm^{-1} in the Raman spectrum of the PVP/MoS_2/RGO sample, which indicate the presence of 1T phase MoS_2. [30,40].

The structural characteristics of pure MoS_2, MoS_2/PVP, and MoS_2/PVP/RGO were investigated using XRD, as shown in Fig. 3f. The pattern for the pure MoS_2 is in good agreement with the 2H-MoS_2 hexagonal structure (JCPDS card No. 37–1492). The strong (0 0 2) diffraction peak implies a well-stacked layered structure along the c-axis. The weaker (0 0 2) diffraction peak and the near-absence of high-indexed diffraction peaks for the MoS_2/PVP and the MoS_2/PVP/RGO samples indicate a low degree of MoS_2 layers stacking,[24] in agreement with the HRTEM imaging results. As shown in the inset of Fig. 3f, in comparison to the pure MoS_2, the (0 0 2) diffraction peaks shift to a lower value for the MoS_2/PVP and the MoS_2/PVP/RGO samples, being consistent with HRTEM results of expanded interlayer spacing.

3.2. HER Electrocatalytic Performance

We investigated the HER performance of MoS_2, MoS_2/PVP, and MoS_2/PVP/RGO samples fabricated by inkjet printing. The schematic diagram and optical microscope image of a planar sample with catalysts evenly printed on Cu film are displayed in Fig. 4**a**. The overpotential (at 10 mA cm^{-2} current density) of the MoS_2/PVP catalyst is much smaller than that of the pure MoS_2 catalyst, and that of the MoS_2/PVP/RGO catalyst decreases even further (Fig. 4b). Meanwhile, the slope obtained from the linear portion of the Tafel plot exhibits the same variation trend (Fig. 4c). These results indicate that the participation of PVP and RGO significantly improves the catalytic activity of MoS_2 nanostructures for HER. To explore the influence of edge site exposure on catalytic performance, we designed and fabricated a 3D spatially-structured configuration of catalysts by inkjet printing. The schematic diagram and optical microscope image of a patterned sample are shown in Fig. 4d. The uneven distribution of catalysts in the plane direction is evident from the optical image. The patterned catalysts demonstrate a better HER activity than the planar catalysts, as summarized in **Table S1**. In particular, the patterned MoS_2/PVP/RGO on Cu film only needs 51 mV to drive a current density of 10 mA cm^{-2}, and its Tafel slope is as low as 32 mV dec^{-1}, which is comparable to the Pt/C electrode (the catalytic performance of 20 % Pt/C catalyst on the glassy-carbon electrode is shown in Fig. 4e,f). The HER exchange current density (j_0) for patterned

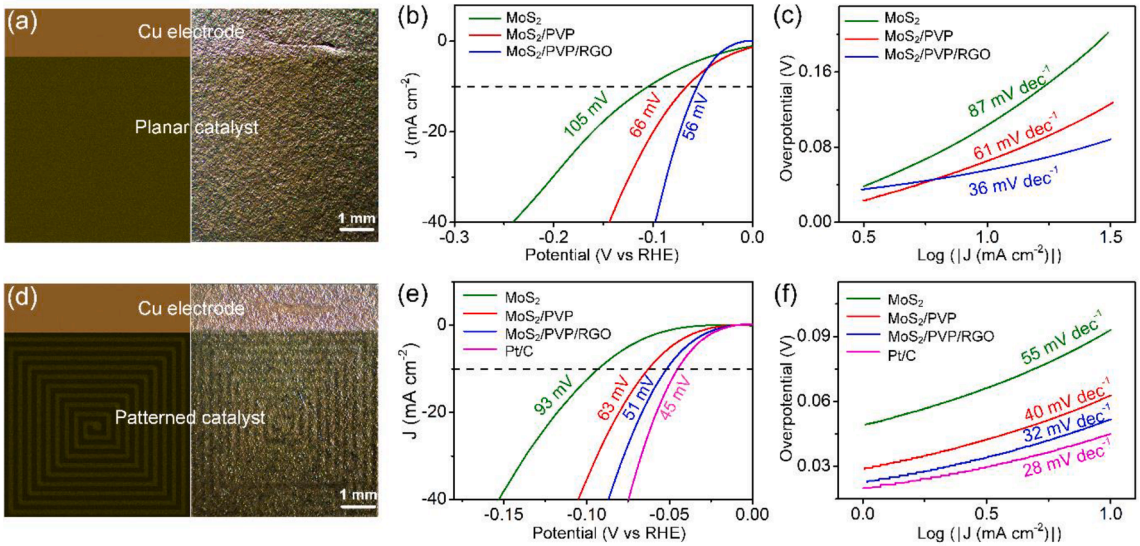

Fig. 4. (a) Schematic diagram (left) and optical microscope image (right) of planar catalyst, (b) polarization curves and (c) Tafel plots of MoS_2, MoS_2/PVP and MoS_2/PVP/RGO planar catalysts, (d) schematic diagram (left) and optical microscope image (right) of patterned catalyst, (e) polarization curves and (f) Tafel plots of MoS_2, MoS_2/PVP and MoS_2/PVP/RGO patterned catalysts (Pt/C catalyst on glass carbon electrode as a reference).

MoS_2/PVP/RGO on Cu film is 0.267 mA cm^{-2}, as deduced from the Tafel plot using the extrapolation method.

Cyclic voltammetry (CV) experiments were carried out to obtain the electrochemical double-layer capacitance (C_{dl}) of catalytic electrodes, which can be used to evaluate the electrochemical surface area (ECSA) of the catalyst.[57] CV curves of planar and patterned electrodes are shown in **Figs. S5 and S6**, respectively. The halves of the maximum and minimum current density differences at the center of the scanning potential range are plotted versus the voltage scan rates in Fig. 5**a and 5b**, in which the slopes correspond to C_{dl} values. For planar catalysts, the C_{dl} values of MoS_2/PVP and MoS_2/PVP/RGO are about twice as much as that of the pure MoS_2, while patterned catalysts show much higher C_{dl} values compared with planar catalysts. The high ECSA for patterned MoS_2/PVP/RGO catalyst implies a larger number of active sites, consistent with the improved catalytic performance. The outstanding HER activity of Cu-supported MoS_2/PVP/RGO catalyst is further demonstrated in Fig. 5c, in which an ultrahigh cathodic current density of 3250 mA cm^{-2} is achieved at 600 mV.

The catalytic kinetics of patterned MoS_2, MoS_2/PVP, and MoS_2/PVP/RGO electrodes were investigated by electrochemical impedance spectroscopy (EIS), as shown in Fig. 5d. Compared with the pure MoS_2 and the MoS_2/PVP, the MoS_2/PVP/RGO catalyst exhibits the smallest semicircle in the Nyquist plot, indicating the lowest charge-transfer impedance (R_{ct}). The low R_{ct} of the MoS_2/PVP/RGO catalyst allows the fast shuttling of electrons during HER. DFT calculation results suggested a strong electronic coupling at the interface between MoS_2 and RGO with polydopamine (PDA) as a linker.[58] It is expected that electronic coupling also exists in the MoS_2/PVP/RGO hybrid due to the similar functionality of PVP and PDA. Thus, for the hybrid MoS_2/PVP/RGO system integrated on Cu films, it can be considered a Cu-RGO-MoS_2 contact (MoS_2/PVP on Cu film can be considered a Cu-MoS_2 contact). It was demonstrated that RGO between metal and MoS_2 could significantly reduce the contact resistance and enhance electron injection into the conduction band of MoS_2.[59,60].

To take advantage of the capabilities offered by inkjet printing, different graphic patterns (first printing 10 passes to form a plane, and then printing 10 passes more to generate a 3D spatial pattern on the plane) were fabricated, as shown in Fig. 6**a-d**. All samples were prepared using MoS_2/PVP/RGO ink. Polarization curves and Tafel plots of samples with different graphic patterns are depicted in Fig. 6e and 6f, respectively. It is clearly shown that the electrode with a square-spiral design displays the highest activity towards HER with minimum overpotential and Tafel slope. Electrochemical cyclic voltammograms of MoS_2/PVP/RGO samples with different patterns are shown in **Fig. S7**, and the corresponding C_{dl} values can be found in Fig. 6g. The C_{dl} of the square-spiral pattern is the highest, which means that the electrochemical effective surface area of this electrode is maximum. Obviously, an optimized spatial configuration can provide a larger specific surface area to expose a higher amount of edge sites.

Further, different printing passes for forming the square-spiral spatial pattern were carried out using MoS_2/PVP/RGO ink (**Fig. S8a**, **10** printing passes for the underneath plane layer were done before the formation of the square-spiral pattern). Polarization curves and Tafel plots of the corresponding catalytic electrodes are shown in **Fig. S8b and S8c**, respectively. It can be seen that the patterned catalyst with 10 passes shows the highest activity towards the HER. CV curves and the corresponding C_{dl} values of patterned catalysts prepared with different passes are shown in **Fig. S9**. It confirms that the HER activity of the catalysts with 0-pass and 5-pass patterns is limited by a lower ECSA. Although the 15-pass and 20-pass patterned catalysts have higher ECSA, the lower HER activity can be attributed to the decrease of charge transfer efficiency with the increase of catalyst thickness.

DFT calculations were employed to reveal the role of RGO in the catalyst system. Cu (1 1 1) plane was exposed to build contact structures, and the top view of Cu-MoS_2 and Cu-RGO-MoS_2 models are shown in Fig. 7**a and 7c**, respectively. The electronic band structures of these two contacts are displayed in Fig. 7b and 7e. It can be clearly seen that the band gap of Cu-MoS_2 is about 2.61 eV, while the band gap of Cu-RGO-MoS_2 disappears showing metallic properties. The total and partial density of states were further calculated to analyze the interaction

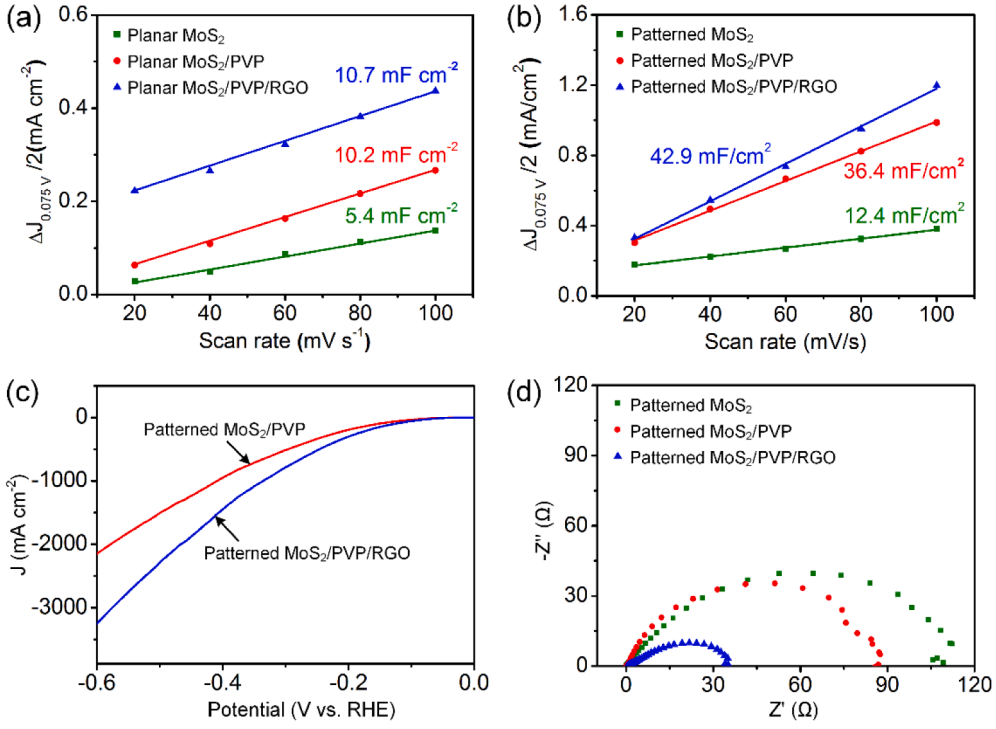

Fig. 5. Curves of capacitive currents versus scan rates for (a) planar catalysts and (b) patterned catalysts by electrochemical double-layer capacitance measurements. (c) Polarization curves of patterned MoS_2/PVP and MoS_2/PVP/RGO catalyst to achieve very high cathodic current density. (d) EIS plots of MoS_2, MoS_2/PVP and MoS_2/PVP/RGO patterned catalysts.

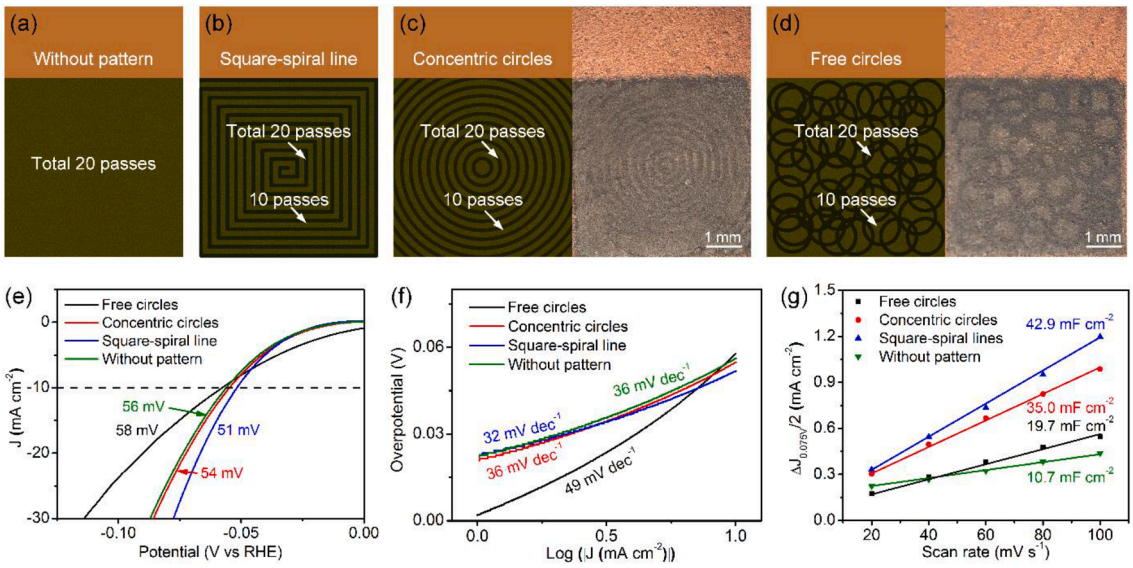

Fig. 6. Schematic diagrams and optical microscope images of catalytic electrode (a) without pattern, (b) with square-spiral line pattern, (c) with concentric circles, and (d) with free circles. (e) Polarization curves, (f) Tafel plots, and (g) Curves of capacitive currents versus scan rates of samples with different pattern. All samples were prepared by using MoS_2/PVP/RGO ink.

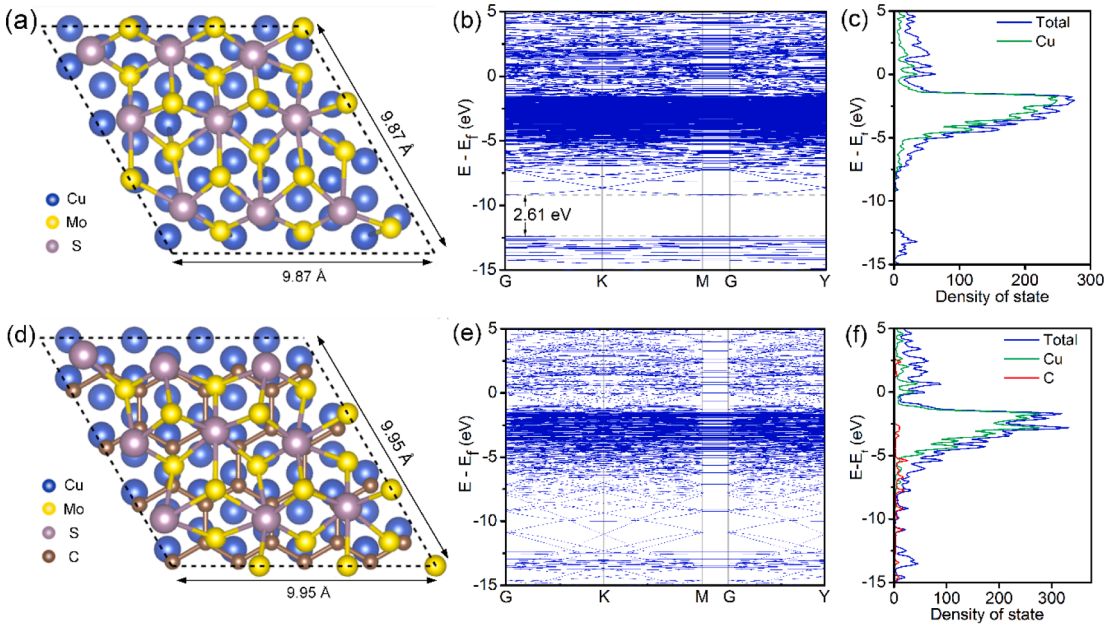

Fig. 7. (a) Top view of Cu-MoS_2 contact. Here blue, yellow and purple balls denote Cu, Mo and S atoms, respectively. Atoms beyond the boundary are not shown. (b) Electronic band structure and (c) total density of states (TDOS) and partial density of states (PDOS) from Cu of Cu-MoS_2 contact. (d) Top view of Cu-RGO-MoS_2 contact. Here blue, yellow, purple and brown balls denote Cu, Mo, S and C atoms, respectively. Atoms beyond the boundary are not shown. (e) Electronic band structure of Cu-RGO-MoS_2 contact. (f) TDOS and PDOS from C and Cu of Cu-RGO-MoS_2 contact.

mechanism of different components, as shown in Fig. 7c for Cu-MoS_2 and Fig. 7f for Cu-RGO-MoS_2. From the comparison of these two results, it can be seen that the C atoms from RGO introduce electronic states into the energy band, resulting in the disappearance of the band gap of Cu-RGO-MoS_2. As a conductor, Cu only contributes to the electronic states of the conduction band rather than introducing extra energy levels into the band gap. Based on the above discussion, it can be inferred that the introduction of RGO between Cu support and MoS_2 catalysts enhances the conductive capability, enhancing the electron transfer between the Cu film and the edge sites and giving rise to a high electron injection efficiency.

Per-site turnover frequency (TOF) is a crucial parameter to estimate the intrinsic activities of a catalyst for HER.[61,62] To evaluate the intrinsic HER kinetic of the patterned MoS_2/PVP/RGO catalyst, we investigate its TOF through an electrochemical approach (see the calculation details in Supporting Information).[63] The TOF curve derived from the polarization curve and the ECSA is plotted in Fig. 8**a**. We obtained a high intrinsic activity with 1.14 s^{-1} per site at 200 mV overpotential.

In addition to HER activity, stability is a significant criterion for evaluating a catalyst's performance. To assess the stability of the patterned MoS_2/PVP/RGO catalyst, we performed long-term potential sweeps for 5000 cycles (taking RHE as a reference). As shown in Fig. 8b, the polarization curve of the catalyst after 5000 cycles exhibits

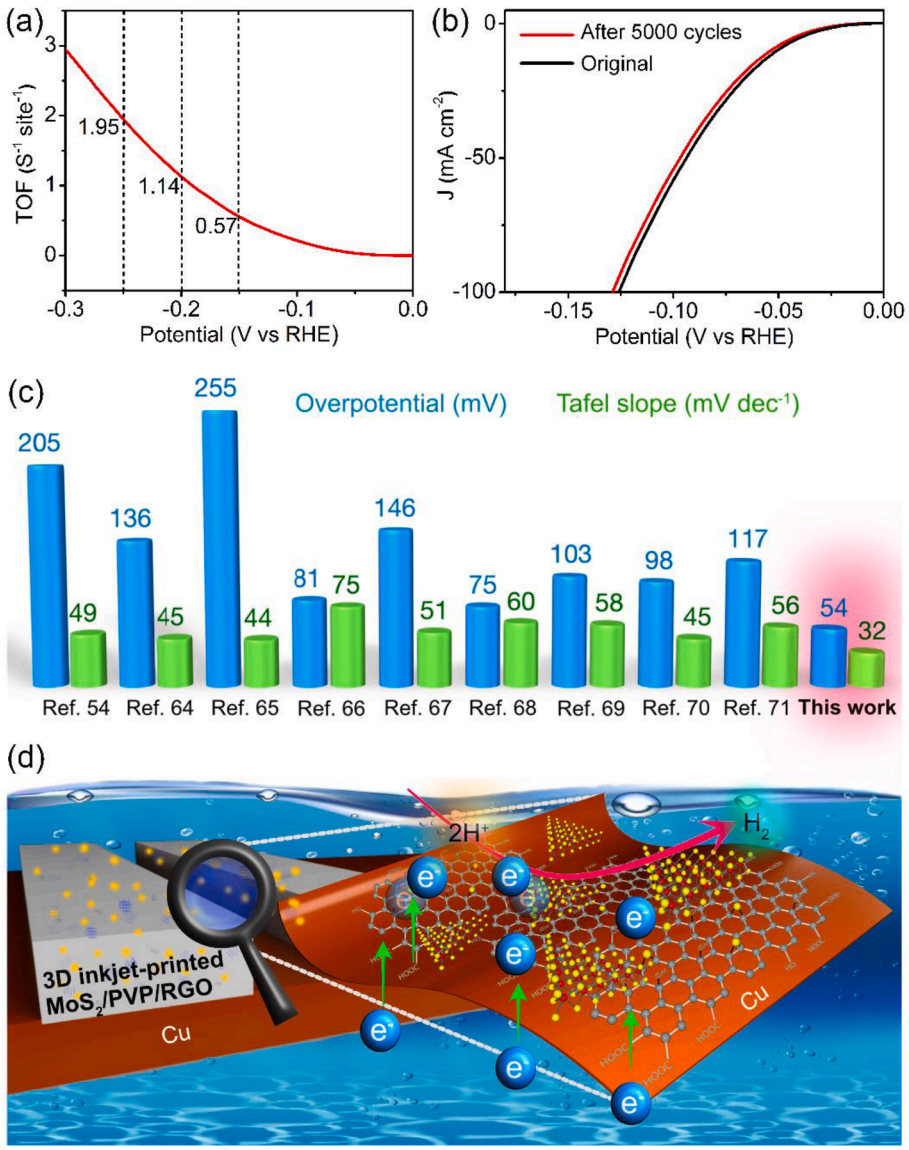

Fig. 8. (a) TOF curve of the patterned MoS_2/PVP/RGO catalyst (plotted from the polarization curve and the ECSA). (b) Polarization curves of patterned MoS_2/PVP/RGO catalyst before and after 5000 cycles. (c) Comparison of the overpotentials at 10 mA cm^{-2} and Tafel slopes for various TMDs catalysts. (d) Illustration of the HER process of MoS_2 nanostructures surrounded by RGO on Cu film.

negligible current degradation compared to the original one, which proves exceptional durability. There is almost no change in the morphology of the catalyst before and after the stability test (Fig. S10). In addition, the superior HER performance of the catalyst is verified again due to the low overpotential of 126 mV to drive a current density of 100 mA cm^{-2}.

3.3. HER mechanism of patterned MoS_2/PVP/RGO catalyst on Cu film. The overpotential at 10 mA cm^{-2} is a critical factor for HER activity, which is considered a device-oriented total electrode activity metric.[61] Besides, the Tafel slope reflects the HER reaction kinetics. A low Tafel slope is preferred since it implies a rapid increase in hydrogen generation rate at the applied overpotential. As mentioned above, the patterned MoS_2/PVP/RGO catalyst on Cu film shows very low overpotential and Tafel slope values that are close to those of the Pt/C electrode. The overpotentials required to reach 10 mA cm^{-2} and the Tafel slopes of recently developed TMDs-based electrocatalysts are summarized in Fig. 8c (detailed information is shown in Table S2), including WS_2/Ni_5P_4-Ni_2P,[11] monolayers MoS_2/porous carbon,[64] $MoSe_2/MoO_2$ hybrid,[65] $MoS_2/CoNi_2S_4$,[66] Co_9S_8/MoS_2 core/shell nanocrystals,[67] MoSSe nanodots,[68] graphdiyne/MoS_2,[69] $MoSe_2$-based heterostructures,[70] and WS_2@graphene.[71] To the best of our knowledge, the overpotential and the Tafel slope of patterned MoS_2/PVP/RGO catalyst on Cu film outperform most results reported for TMDs. For the HER in acidic media, three principal reaction steps were suggested.[72] First is a primary discharge step (equation (1), Tafel slope of about 120 mV dec^{-1}). This step is followed by either an electrochemical desorption step (equation (2), Tafel slope of about 40 mV dec^{-1}) or a recombination step (equation (3), Tafel slope of about 30 mV dec^{-1}).

$$Volmer\ reaction:\ H_3O^+ + e^- \rightarrow H_{ads} + H_2O \quad (1)$$

$$Heyrovsky\ reaction:\ H_{ads} + H_3O^+ + e^- \rightarrow H_2 + H_2O \quad (2)$$

$$Tafel\ reaction:\ H_{ads} + H_{ads} \rightarrow H_2 \quad (3)$$

Here, H_{ads} represents the hydrogen adsorption sites onto the surface of a catalyst. The Tafel slope of 32 mV dec^{-1} for the patterned MoS_2/PVP/RGO on Cu film suggests that HER proceeds through a rapid Volmer reaction followed by a rate-limiting Tafel step. The improved electronic coupling and fast shuttling of electrons discussed above

contribute to the fast proton discharge kinetic.

Based on the above investigations, the high catalytic performance of patterned MoS_2/PVP/RGO on Cu film could be attributed to the following reasons schematically described in Fig. 8d. (i) Nanoscopic few-layer MoS_2 contributes to the abundant active sites, and 3D configurations formed by inkjet printing help to increase the density of exposed active edges. (ii) The 2H-to-1T conversion of MoS_2 and the reduced charge-transfer impedance originated in RGO surrounding MoS_2, both support fast HER kinetics. (iii) Cu film contacted to MoS_2 with RGO interlayer allows the efficient electron injection from the electrode to MoS_2.

4. Conclusion

We demonstrated a facile and scalable approach to achieve an all-in-one MoS_2-based electrocatalyst for ultra-efficient hydrogen evolution. The 3D patterned MoS_2/PVP/RGO catalyst with partial 1 T-MoS_2 and spatial configuration was constructed on Cu support by inkjet printing, which exhibited excellent catalytic performance with exceptionally low overpotential (51 mV at 10 mA cm^{-2}, 126 mV at 100 mA cm^{-2}), very low Tafel slope (32 mV dec^{-1}), and ultrahigh cathodic current density. These state-of-the-art HER activities benefit from the increased exposure of abundant active sites, reduced charge-transfer impedance, and enhanced electron injection from the contact electrode. The catalytic materials are formulated as an ink for printing, allowing the flexible deposition of the catalysts in spatial patterns, on large areas, on various substrates, and with high throughput, which is an essential step toward industrial applications. This technology provides a new way to design 2D layered-based catalysts for the ultra-efficient electrochemical generation of hydrogen.

Declaration of Competing Interest

The authors declare that they have no known competing financial interests or personal relationships that could have appeared to influence the work reported in this paper.

Data availability

Data will be made available on request.

Acknowledgments

This work was supported by the RFBR and Austrian Science Fond FWF 19-52-14006, and the Sichuan Science and Technology Program (grant No 2023YFG0215). We thank Dr. Enrico Sowade for his valuable contribution to the initiation of this work.

Appendix A. Supplementary data

Supplementary data to this article can be found online at https://doi.org/10.1016/j.cej.2023.141289.

References

[1] M.S. Dresselhaus, I.L. Thomas, Alternative Energy Technologies, Nature 414 (2001) 332–337.
[2] G.W. Crabtree, M.S. Dresselhaus, M.V. Buchanan, The Hydrogen Economy, Phys. Today 57 (12) (2004) 39–44.
[3] S. Chu, A. Majumdar, Opportunities and Challenges for a Sustainable Energy Future, Nature 488 (7411) (2012) 294–303.
[4] M.G. Walter, E.L. Warren, J.R. McKone, S.W. Boettcher, Q. Mi, E.A. Santori, N. S. Lewis, Solar Water Splitting Cells, Chem. Rev. 110 (11) (2010) 6446–6473.
[5] D. He, H. Tang, Z. Kou, M. Pan, X. Sun, J. Zhang, S. Mu, Engineered Graphene Materials: Synthesis and Applications for Polymer Electrolyte Membrane Fuel Cells, Adv. Mater. 29 (20) (2017) 1601741.
[6] R. Gusmão, Z. Sofer, M. Pumera, Exfoliated Layered Manganese Trichalcogenide Phosphite ($MnPX_3$, X = S, Se) as Electrocatalytic van der Waals Materials for Hydrogen Evolution, Adv. Funct. Mater. 29 (2) (2019) 1805975.
[7] N. Cheng, S. Stambula, D. Wang, M.N. Banis, J. Liu, A. Riese, B. Xiao, R. Li, T. K. Sham, L.M. Liu, G.A. Botton, X. Sun, Platinum Single-Atom and Cluster Catalysis of the Hydrogen Evolution Reaction, Nat. Commun. 7 (2016) 13638.
[8] N. Ran, W. Qiu, E. Song, Y. Wang, X. Zhao, Z. Liu, J. Liu, Bond Electronegativity as Hydrogen Evolution Reaction Catalyst Descriptor for Transition Metal (TM=Mo, W) Dichalcogenides, Chem. Mater. 32 (3) (2020) 1224–1234.
[9] C. Meerbach, B. Klemmed, D. Spittel, C. Bauer, Y.J. Park, R. Hübner, H.Y. Jeong, D. Erb, H.S. Shin, V. Lesnyak, A. Eychmüller, General Colloidal Synthesis of Transition-Metal Disulfide Nanomaterials as Electrocatalysts for Hydrogen Evolution Reaction, ACS Appl. Mater. Interfaces 12 (2020) 13148–13155.
[10] T.P. Nguyen, S.Y. Kim, T.H. Lee, H.W. Jang, Q.V. Le, I.T. Kim, Facile Synthesis of $W_2C@WS_2$ Alloy Nanoflowers and Their Hydrogen Generation Performance, Appl. Surf. Sci. 504 (2020), 144389.
[11] L. Song, X. Zhang, S. Zhu, Y. Xu, Y. Wang, Hydrogen Spillover Effect Enhanced by Carbon Quantum Dots Activated MoS_2, Carbon 199 (2022) 63–69.
[12] S. Chen, Y. Pan, Enhancing Catalytic Properties of Noble Metal@MoS_2/WS_2 Heterojunction for the Hydrogen Evolution Reaction, Appl. Surf. Sci. 591 (2022), 153168.
[13] V.T. Nguyen, P.A. Le, Y.C. Hsu, K.H. Wei, Plasma-Induced Exfoliation Provides Onion-Like Graphene-Surrounded MoS_2 Nanosheets for a Highly Efficient Hydrogen Evolution Reaction, ACS Appl. Mater. Interfaces 12 (2020) 11533–11542.
[14] S. Balasubramanyam, M. Shirazi, M.A. Bloodgood, L. Wu, M.A. Verheijen, V. Vandalon, W.M.M. Kessels, J.P. Hofmann, A.A. Bol, Edge-Site Nanoengineering of WS_2 by Low-Temperature Plasma Enhanced Atomic Layer Deposition for Electrocatalytic Hydrogen Evolution, Chem. Mater. 31 (14) (2019) 5104–5115.
[15] H.I. Karunadasa, E. Montalvo, Y. Sun, M. Majda, J.R. Long, C.J. Chang, A Molecular MoS_2 Edge Site Mimic for Catalytic Hydrogen Generation, Science 335 (6069) (2012) 698–702.
[16] G. Li, C. Fu, J. Wu, J. Rao, S. Liou, X. Xu, B. Shao, K. Liu, E. Liu, N. Kumar, X. Liu, M. Fahlman, J. Gooth, G. Auffermann, Y. Sun, C. Felser, B. Zhang, Synergistically Creating Sulfur Vacancies in Semimetal-Supported Amorphous MoS_2 for Efficient Hydrogen Evolution, Appl. Catal. B 254 (2019) 1–6.
[17] X. Li, S. Guo, W. Li, X. Ren, J. Su, Q. Song, A.J. Sobrido, B. Wei, Edge-rich MoS_2 Grown on Edge-oriented Three-dimensional Graphene Glass for High-performance Hydrogen Evolution, Nano Energy 57 (2019) 388–397.
[18] Y. Zhou, J. Zhang, E. Song, J. Lin, J. Zhou, K. Suenaga, W. Zhou, Z. Liu, J. Liu, J. Lou, H.J. Fan, Enhanced Performance of In-plane Transition Metal Dichalcogenides Monolayers by Configuring Local Atomic Structures, Nat. Commun. 11 (2020) 2253.
[19] X. Wang, J. Wang, B. Wei, N. Zhang, J. Xu, H. Miao, L. Liu, C. Su, Y. Li, Z. Wang, Plasma Tailoring in WTe_2 Nanosheets for Efficiently Boosting Hydrogen Evolution Reaction, J. Mater. Sci. Technol. 78 (2021) 170–175.
[20] M. Wang, L.i. Zhang, Y. He, H. Zhu, Recent Advances in Transition-metal-sulfide-based Bifunctional Electrocatalysts for Overall Water Splitting, J. Mater. Chem. A 9 (9) (2021) 5320–5363.
[21] H.G. Shiraz, X. Crispin, M. Berggren, Transition Metal Sulfides for Electrochemical Hydrogen Evolution, Int. J. Hydrogen. Energ. 46 (2021) 24060–24077.
[22] T. Wang, L. Liu, Z. Zhu, P. Papakonstantinou, J. Hu, H. Liu, M. Li, Enhanced Electrocatalytic Activity for Hydrogen Evolution Reaction from Self-Assembled Monodispersed Molybdenum Sulfide Nanoparticles on an Au Electrode, Energy Environ. Sci. 6 (2) (2013) 625–633.
[23] H. Cheng, Y. Diao, Q. Liu, L. Wei, X. Li, J. Chen, F. Wang, Di-nuclear Metal Synergistic Catalysis: $Ni_2Mo_6S_6O_2$/MoS_2 Two-dimensional Nanosheets for Hydrogen Evolution Reaction, Chem. Eng. J. 428 (2022), 131084.
[24] I.S. Amiinu, Z. Pu, X. Liu, K.A. Owusu, H.G.R. Monestel, F.O. Boakye, H. Zhang, S. Mu, Multifunctional Mo-N/C@MoS_2 Electrocatalysts for HER, OER, ORR, and Zn-Air Batteries, Adv. Funct. Mater. 27 (44) (2017) 1702300.
[25] Y. Liu, X. Xu, J. Zhang, H. Zhang, W. Tian, X. Li, M.O. Tade, H. Sun, S. Wang, Flower-like MoS_2 on Graphitic Carbon Nitride for Enhanced Photocatalytic and Electrochemical Hydrogen Evolutions, Appl. Catal. B 239 (2018) 334–344.
[26] S. Bolar, S. Shit, J.S. Kumar, N.C. Murmu, R.S. Ganesh, H. Inokawa, T. Kuila, Optimization of Active Surface Area of Flower like MoS_2 Using V-Doping towards Enhanced Hydrogen Evolution Reaction in Acidic and Basic Medium, Appl. Catal. B 254 (2019) 432–442.
[27] X. Ren, L. Pang, Y. Zhang, X. Ren, H. Fan, S. Liu, One-Step Hydrothermal Synthesis of Monolayer MoS_2 Quantum Dots for Highly Efficient Electrocatalytic Hydrogen Evolution, J. Mater. Chem. A 3 (20) (2015) 10693–10697.
[28] J. Kibsgaard, Z. Chen, B.N. Reinecke, T.F. Jaramillo, Engineering the Surface Structure of MoS_2 to Preferentially Expose Active Edge Sites for Electrocatalysis, Nat. Mater. 11 (2012) 963–969.
[29] Y. Liu, X. Zhou, T. Ding, C. Wang, Q. Yang, 3D Architecture Constructed via Confined Growth of MoS_2 Nanosheets in Nanoporous Carbon Derived from Metal-Organic Frameworks for Efficient Hydrogen Production, Nanoscale 7 (43) (2015) 18004–18009.
[30] H. Wang, Z. Lu, D. Kong, J. Sun, T.M. Hymel, Y. Cui, Electrochemical Tuning of MoS_2 Nanoparticles on Three-Dimensional Substrate for Efficient Hydrogen Evolution, ACS Nano 8 (5) (2014) 4940–4947.
[31] Q. Liu, Q. Fang, W. Chu, Y. Wan, X. Li, W. Xu, M. Habib, S. Tao, Y. Zhou, D. Liu, T. Xiang, Electron-Doped 1T-MoS_2 via Interface Engineering for Enhanced Electrocatalytic Hydrogen Evolution, Chem. Mater. 29 (11) (2017) 4738–4744.
[32] C. Jian, W. Hong, Q. Cai, J. Li, W. Liu, Surface Electron State Engineering Enhanced Hydrogen Evolution of Hierarchical Molybdenum Sisulfide in Acidic and Alkaline Media, Appl. Catal. B 266 (2020), 118649.

[33] Y. Guo, K. Xu, C. Wu, J. Zhao, Y. Xie, Surface Chemical-Modification for Engineering the Intrinsic Physical Properties of Inorganic Two-Dimensional Nanomaterials, Chem. Soc. Rev. 44 (3) (2015) 637–644.
[34] Y. Yu, S.Y. Huang, Y. Li, S.N. Steinmann, W. Yang, L. Cao, Layer-Dependent Electrocatalysis of MoS_2 for Hydrogen Evolution, Nano Lett. 14 (2) (2014) 553–558.
[35] J. Xie, J. Zhang, S. Li, F. Grote, X. Zhang, H. Zhang, R. Wang, Y. Lei, B. Pan, Y. Xie, Controllable Disorder Engineering in Oxygen-Incorporated MoS_2 Ultrathin Nanosheets for Efficient Hydrogen Evolution, J. Am. Chem. Soc. 135 (47) (2013) 17881–17888.
[36] L. Ma, Y. Hu, G. Zhu, R. Chen, T. Chen, H. Lu, Y. Wang, J. Liang, H. Liu, C. Yan, Z. Tie, Z. Jin, J. Liu, In Situ Thermal Synthesis of Inlaid Ultrathin MoS_2/Graphene Nanosheets as Electrocatalysts for the Hydrogen Evolution Reaction, Chem. Mater. 28 (26) (2016) 5733–5742.
[37] J. Joyner, E.F. Oliveira, H. Yamaguchi, K. Kato, S. Vinod, D.S. Galvao, D. Salpekar, S. Roy, U. Martinez, C.S. Tiwary, S. Ozden, P.M. Ajayan, Graphene Supported MoS2 Structures with High Defect Density for an Efficient HER Electrocatalysts, ACS Appl. Mater. Interfaces 12 (2020) 12629–12638.
[38] Z.H. Deng, L. Li, W. Ding, K. Xiong, Z.D. Wei, Synthesized Ultrathin MoS_2 Nanosheets Perpendicular to Graphene for Catalysis of Hydrogen Evolution Reaction, Chem. Commun. 51 (10) (2015) 1893–1896.
[39] D. Huang, L. Lei, R. Deng, S. Chen, Z. Li, C. Zhang, W. Wang, K. Wang, The Synergistic eEffect of Proton Intercalation and Electron Transfer via Electro-activated Molybdenum Disulfide/graphite Felt toward Hydrogen Evolution Reaction, J. Catal. 381 (2020) 175–185.
[40] H. Wang, Z. Lu, S. Xu, D. Kong, J.J. Cha, G. Zheng, P.C. Hsu, K. Yan, D. Bradshaw, F.B. Prinz, Y. Cui, Electrochemical Tuning of Vertically Aligned MoS_2 Nanofilms and Its Application in Improving Hydrogen Evolution Reaction, PNAS 110 (49) (2013) 19701–19706.
[41] B. Gao, X. Du, Y. Li, S. Ding, C. Xiao, Z. Song, Deep Phase Transition of MoS_2 for Excellent Hydrogen Evolution Reaction by a Facile C-Doping Strategy, ACS Appl. Mater. Interfaces 12 (2020) 877–885.
[42] X.u. Xin, Y. Song, S. Guo, Y. Zhang, B. Wang, J. Yu, X. Li, In-situ Growth of High-content 1T Phase MoS_2 Confined in the CuS Nanoframe for Efficient Photocatalytic Hydrogen Evolution, Appl. Catal. B 269 (2020) 118773.
[43] C. Tsai, F. Abild-Pedersen, J.K. Nørskov, Tuning the MoS_2 Edge-Site Activity for Hydrogen Evolution via Support Interactions, Nano Lett. 14 (3) (2014) 1381–1387.
[44] D. Voiry, R. Fullon, J. Yang, C.C.C. e, de Silva, R. Kappera, I. Bozkurt, D. Kaplan, M. J. Lagos, P.E. Batson, G. Gupta, A.D. Mohite, L. Dong, D. Er, V.B. Shenoy, T. Asefa, M. Chhowalla, The Role of Electronic Coupling between Substrate and 2D MoS_2 Nanosheets in Electrocatalytic Production of Hydrogen, Nature Mater. 15 (2016) 1003–1009.
[45] X. Geng, W. Wu, N. Li, W. Sun, J. Armstrong, A. Al-hilo, M. Brozak, J. Cui, T. Chen, Three-Dimensional Structures of MoS_2 Nanosheets with Ultrahigh Hydrogen Evolution Reaction in Water Reduction, Adv. Funct. Mater. 24 (39) (2014) 6123–6129.
[46] J. Li, C. Zhang, H. Ma, T. Wang, Z. Guo, Y. Yang, Y. Wang, H. Ma, Modulating Interfacial Charge Distribution of Single Atoms Confined in Molybdenum Phosphosulfide Heterostructures for High Efficiency Hydrogen Evolution, Chem. Eng. J. 414 (2021), 128834.
[47] Z. Zhang, W. Li, M.F. Yuen, T.W. Ng, Y. Tang, C.S. Lee, X. Chen, W. Zhang, Hierarchical Composite Structure of Few-Layers MoS_2 Nanosheets Supported by Vertical Graphene on Carbon Cloth for High-performance Hydrogen Evolution Reaction, Nano Energy 18 (2015) 196–204.
[48] X. Wang, X. Gan, T. Hu, K. Fujisawa, Y. Lei, Z. Lin, B. Xu, Z.H. Huang, F. Kang, M. Terrones, R. Lv, Noble-Metal-Free Hybrid Membranes for Highly Efficient Hydrogen Evolution, Adv. Mater. 29 (4) (2017) 1603617.
[49] H.B. Michaelson, Work Function of Elements and Its Periodicity, J. Appl. Phys. 48 (11) (1977) 4729–4933.
[50] W. Wang, Y. Liu, L. Tang, Y. Jin, T. Zhao, F. Xiu, Controllable Schottky Barriers between MoS_2 and Permalloy, Sci. Rep. 4 (2014) 6928.
[51] Y. Wang, H. Guo, J.J. Chen, E. Sowade, Y. Wang, K. Liang, K. Marcus, R. R. Baumann, Z.S. Feng, Paper-Based Inkjet-Printed Flexible Electronic Circuits, ACS Appl. Mater. Interfaces 8 (39) (2016) 26112–26118.
[52] A. Ciesielski, P. Samori, Graphene via Sonication Assisted Liquid-Phase Exfoliation, Chem. Soc. Rev. 43 (1) (2014) 381–398.
[53] Y. Liu, L. Jiao, Q. Wu, Y. Zhao, K. Cao, H. Liu, Y. Wang, H. Yuan, Synthesis of rGO-Supported Layered MoS_2 for High-Performance Rechargeable Mg Batteries, Nanoscale 5 (20) (2013) 9562–9567.
[54] H. Mao, X. Guo, Q. Fan, Y. Fu, H. Yang, D. Liu, S. Wu, Q. Wu, X.-M. Song, Improved Hydrogen Evolution Activity by Unique NiS_2-MoS_2 Heterostructures with Misfit Lattices Supported on Poly(ionic liquid)s Functionalized Polypyrrole/graphene Oxide Nanosheets, Chem. Eng. J. 404 (2021), 126253.
[55] J.G. Choi, L.T. Thompson, XPS Study of As-Prepared and Reduced Molybdenum Oxides, Appl. Surf. Sci. 93 (2) (1996) 143–149.
[56] K.R.G. Lim, A.D. Handoko, L.R. Johnson, T. Fujita, X. Meng, M. Lim, G. S. Subramanian, B. Anasori, Y. Gogotsi, A. Vojvodic, Z.W. She, 2H-MoS_2 on Mo_2CTx MXene Nanohybrid for Efficient and Durable Electrocatalytic Hydrogen Evolution, ACS *Nano* 14 (2020) 16140–16155.
[57] J. Kibsgaard, T.F. Jaramillo, Molybdenum Phosphosulfide: An Active, Acid-Stable, Earth-Abundant Catalyst for the Hydrogen Evolution Reaction, Angew. Chem., Int. Ed. 53 (52) (2014) 14433–14437.
[58] Z. Lei, L. Xu, Y. Jiao, A. Du, Y. Zhang, H. Zhang, Strong Coupling of MoS_2 Nanosheets and Nitrogen-Doped Graphene for High-Performance Pseudocapacitance Lithium Storage, Small 14 (25) (2018) 1704410.
[59] Y. Du, L. Yang, J. Zhang, H. Liu, K. Majumdar, P.D. Kirsch, P.D. Ye, MoS_2 Field-Effect Transistors with Graphene/Metal Heterocontacts, IEEE Electron Device Lett. 35 (5) (2014) 599–601.
[60] W.S. Leoug, X. Luo, Y. Li, K.H. Khoo, S.Y. Quek, J.T.L. Thoug, Low Resistance Metal Contacts to MoS_2 Devices with Nickel-Etched-Graphene Electrodes, ACS Nano 9 (1) (2015) 869–877.
[61] J.D. Benck, T.R. Hellstern, J. Kibsgaard, P. Chakthranont, T.F. Jaramillo, Catalyzing the Hydrogen Evolution Reaction (HER) with Molybdenum Sulfide Nanomaterials, ACS Catal. 4 (11) (2014) 3957–3971.
[62] J. Hu, B. Huang, C. Zhang, Z. Wang, Y. An, D. Zhou, H. Lin, M.K.H. Leung, S. Yang, Engineering Stepped Edge Surface Structures of MoS_2 Sheet Stacks to Accelerate the Hydrogen Evolution Reaction, Energy Environ. Sci. 10 (2) (2017) 593–603.
[63] Z. Zhao, F. Qin, S. Kasiraju, L. Xie, M.K. Alam, S. Chen, D. Wang, Z. Ren, Z. Wang, L.C. Grabow, J. Bao, Vertically Aligned MoS_2/Mo_2C Hybrid Nanosheets Grown on Carbon Paper for Efficient Electrocatalytic Hydrogen Evolution, ACS Catal. 7 (10) (2017) 7312–7318.
[64] J. Li, A. Listwan, J. Liang, F. Shi, K. Li, J. Jia, High Proportion of 1 T Phase MoS_2 Prepared by a Simple Solvothermal Method for High-efficiency Electrocatalytic Hydrogen Evolution, Chem. Eng. J. 422 (2021), 130100.
[65] H. Li, X. Han, S. Jiang, L. Zhang, W. Ma, R. Ma, Z. Zhou, Controllable Fabrication and Structure Evolution of Hierarchical 1T-MoS_2 Nanospheres for Efficient Hydrogen Evolution, Green Energy Environ. 7 (2022) 314–323.
[66] J. Hu, C. Zhang, P. Yang, J. Xiao, T. Deng, Z. Liu, B. Huang, M.K.H. Leung, S. Yang, Kinetic-oriented Construction of MoS_2 Synergistic Interface to Boost pH-Universal Hydrogen Evolution, Adv. Funct. Mater. 30 (6) (2020) 1908520.
[67] Y. Zhang, H. Zhou, H. Wang, Y. Zhang, D.D. Dionysiou, Synergistic Effect of Reduced Graphene Oxide and Near-infrared Light on MoS_2-mediated Electrocatalytic Hydrogen Evolution, Chem. Eng. J. 418 (2021), 129343.
[68] D. Vikraman, S. Hussain, S.A. Patil, L. Truong, A.A. Arbab, S.H. Jeong, S.-H. Chun, J. Jung, H.-S. Kim, Engineering $MoSe_2$/WS_2 Hybrids to Replace the Scarce Platinum Electrode for Hydrogen Evolution Reactions and Dye-Sensitized Solar Cells, ACS Appl. Mater. Interfaces 13 (2021) 5061–5072.
[69] M. Shi, Z. Jiang, B. Mei, Y. Li, F. Sun, H. Yu, Y. Xu, Tuning the Hydrogen Evolution Performance of 2D Tungsten Disulfide by Interfacial Engineering, J. Mater. Chem. A 9 (2021) 7059.
[70] X. Li, X. Lv, X. Sun, C. Yang, Y.-Z. Zheng, L. Yang, S. Li, X. Tao, Edge-oriented, High-percentage 1T′-phase MoS_2 Nanosheets Stabilize Ti_3C_2 MXene for Efficient Electrocatalytic Hydrogen Evolution, Appl. Catal. B 284 (2021), 119708.
[71] W. Han, Z. Liu, Y. Pan, G. Guo, J. Zou, Y. Xia, Z. Peng, W. Li, A. Dong, Designing Champion Nanostructures of Tungsten Dichalcogenides for Electrocatalytic Hydrogen Evolution, Adv. Mater. 2002584 (2020).
[72] B.E. Conway, B.V. Tilak, Interfacial Processes Involving Electrocatalytic Evolution and Oxidation of H_2, and the Role of Chemisorbed H, Electrochim. Acta 47 (22–23) (2002) 3571–3594.